INTERNATIONAL JOURNAL FOR NUMERICAL METHODS IN FLUIDS
Int. J. Numer. Meth. Fluids **28**: 1199–1216 (1998)

TOOLS FOR PARAMETER STUDIES IN FLUID DYNAMICS

ANDREW YECKEL*

Department of Chemical Engineering and Materials Science, University of Minnesota, Minneapolis, MN 55455-0132, USA

SUMMARY

Several computational methods to aid analysis of steady state problems in fluid dynamics are demonstrated. These include tracking of selected flow states; computing linearized parameter sensitivities and frequency response to forced parameter perturbations; and determining the topology of a flow by systematically locating critical points of the velocity vector field. The primary concern addressed by these methods is analysis of collections of steady state solutions obtained through parameter studies, rather than analysis of an isolated solution. In this regard, these methods are intended to answer the criticism sometimes made that solutions obtained by numerical methods do not lend insight to parameter effects so easily as do traditional methods. Dip coating, slot coating, and a prototype of forward roll coating (a lid-driven cavity with throughflow) are used to demonstrate application of the methods. © 1998 John Wiley & Sons, Ltd.

1. INTRODUCTION

One trend today in fluid dynamics is towards solving ever larger problems, e.g. three-dimensional flows in complex geometries. This trend naturally follows as a consequence of the continued increase in computing power. The ongoing study of two-dimensional flows remains of interest, however. The current capability of computers is such that it is possible to solve many instances of 2D flows, which makes detailed parameter studies possible. Soon computing power will reach a state where such parameter studies are possible for 3D flows as well. A need exists, therefore, to develop methods to systematically analyze collections of steady states. By doing so we can address in part the remark sometimes heard with regard to numerical solutions 'but I can't see the parameter, the way I can see it when I do a perturbation analysis' (or asymptotic analysis, etc.). Towards this end, this paper presents examples of the application of several tools to facilitate parameter studies in fluid dynamics. Parameter studies can provide insights that help develop the fundamental understanding of the behavior of flows, and allow us to confirm hypotheses suggested by simpler models obtained using traditional methods.

Figure 1 shows the flow domains and boundary conditions of several viscous flows chosen as examples in this paper. Figure 1(a) shows a slot coater, in which liquid is extruded at a specified rate from the slot of the coating die onto a moving substrate, or web. Under favorable circumstances a liquid bridge called the coating bead is established across the gap

* Correspondence to: Department of Chemical Engineering and Materials Science, University of Minnesota, Minneapolis, MN 55455-0132, USA.

CCC 0271–2091/98/181199–18$17.50

Received 21 April 1997
Revised 13 January 1998

between the die and the web, and a steady flow results in which air on the web is replaced by a thin layer of liquid that wets it. Figure 1(b) shows another coating method, commonly referred to as dip coating. In the limit that the coating bath becomes small, the dip coater takes on many characteristics of the slot coater [1]. We refer to this example as the slot-to-dip transition. Figure 1(c) shows a lid-driven cavity with throughflow. Flow enters at the bottom left and exits at the upper right. Top and bottom walls move from left to right. The structure of this flow is in many ways similar to that of a feed-forward roll coater, in which a layer of liquid is transferred from one moving roll to another [2].

In all our examples the flow is single-phase, two-dimensional, Newtonian, and of constant density and viscosity (the methods described below do not require these restrictions, however). The corresponding Navier–Stokes equations are

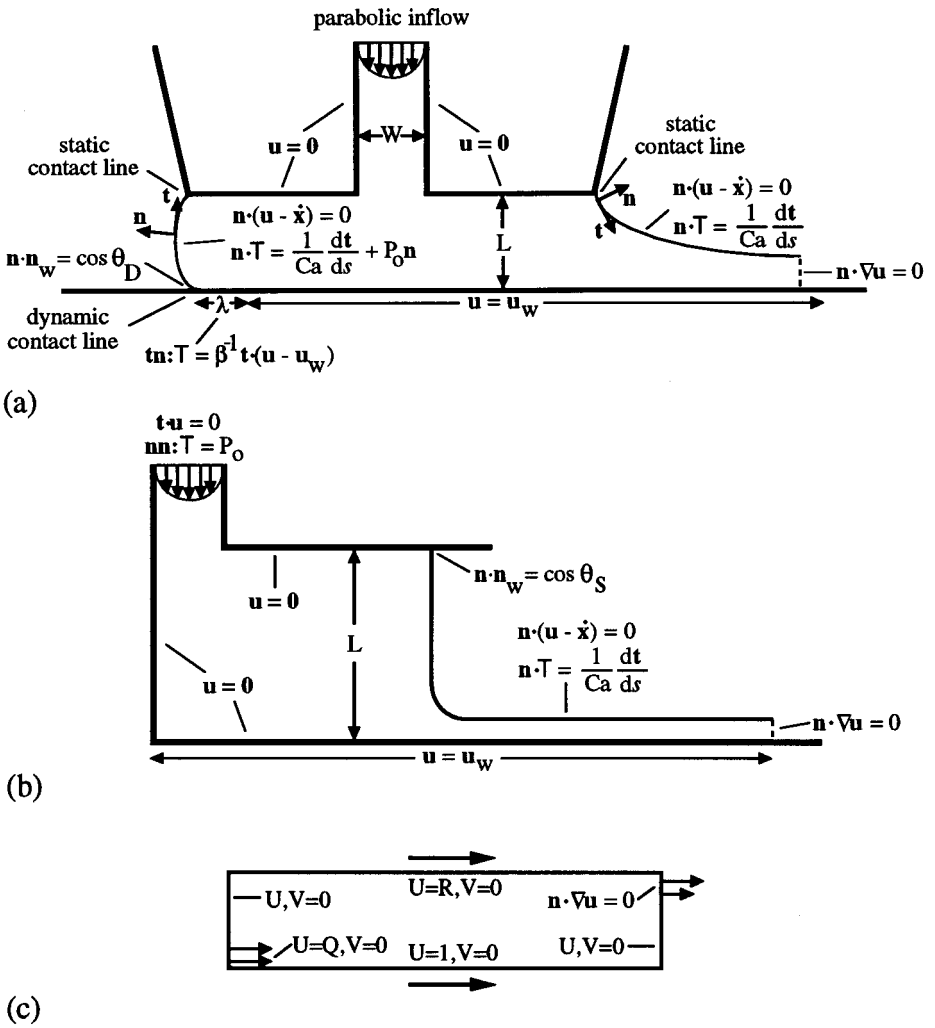

Figure 1. Flow domains and boundary conditions: (a) slot coater; (b) dip coater; (c) lid-driven cavity with throughflow.

$$Re\left[\frac{\partial \mathbf{u}}{\partial t}+\mathbf{u}\cdot\nabla\mathbf{u}\right]=\nabla\cdot\ \top\ +St\mathbf{g},\qquad \nabla\cdot\mathbf{u}=0, \tag{1}$$

where $\top = -p\mathbf{I}+[\nabla\mathbf{u}+(\nabla\mathbf{u})^T]$ is the stress tensor, and $\mathbf{I}$ is the identity tensor. The velocity is $\mathbf{u}$, p is the pressure, and $\mathbf{g}$ is a unit vector in the direction of gravity.

Equation (1) is in dimensionless form. The dimensionless velocity is $\mathbf{u}\equiv\mathbf{u}^*/U$, where U is a characteristic speed (* indicates a dimensional quantity). The Cartesian co-ordinates are $x\equiv x^*/L$ and $y\equiv y^*/L$, where L is a characteristic length. The dimensionless pressure is given by $p\equiv p^*L/\mu U$, where μ is the viscosity. Two dimensionless parameters appear: a Reynolds number, $Re\equiv\rho UL/\mu$, and a Stokes number, $St\equiv\rho gL^2/\mu U$ (ρ is the density and g the gravitational acceleration). The web speed is used as the characteristic velocity in the slot and dip coaters, and the speed of the bottom boundary in the lid-driven cavity. The coating gap is used as the characteristic length in the slot and dip coaters, and the cavity height in the lid-driven cavity.

The boundary conditions that complete the system of equations are summarized in Figure 1. Unit vectors tangent and normal to boundaries are indicated by $\mathbf{t}$ and $\mathbf{n}$, and s is the arc-length along boundaries. Therefore, the curvature of a boundary is equal to $\mathrm{d}\mathbf{t}/\mathrm{d}s$.

When the accompanying air flow is neglected, as in this case, the slot coater has a non-physical singularity at the dynamic wetting line where the upstream free surface attaches to the moving web. To remove the singularity we use Navier's slip condition, which relates the slip velocity to the shear stress at the wall through a slip coefficient β, applied over a slip length λ from the dynamic wetting line. At the inflow boundary a fully developed parabolic velocity profile is imposed. The dimensionless inlet flow rate $Q\equiv Q^*/UL$, is equal to the dimensionless final film thickness, $h\equiv h^*/L$. Fully developed flow is assumed at the outflow, which implies that the normal stress and crosswise velocity are zero. Inflow and outflow boundaries are located at a sufficient distance upstream and downstream, respectively, so that moving either of them further does not appreciably affect the solution in the region of interest. Surface tension σ enters through the normal force balance at free boundaries. The capillary number arises in this boundary condition: $Ca\equiv\mu U/\sigma$. Additional conditions prescribed at free boundaries are vanishing tangential stress, and impenetrability. The impenetrability condition accounts for time-dependent motion of the boundaries, where $\dot{\mathbf{x}}$ is the time rate of change of the boundary position. An apparent contact angle, θ_{D}, is specified at the dynamic contact line. The static contact lines are taken to be pinned at the edges of the die.

The boundary conditions applied to the slot-to-dip transition flows are similar to those of the slot coater, with a few differences. At the inlet, a value P_o is specified for the normal stress, and the crosswise velocity is set to zero. At the static contact line two conditions are considered: either the contact line is pinned, as in the case of the slot coater, or the static contact angle at which the free surface meets the wall is set to a value θ_{S}.

In the lid-driven cavity, no-slip and impenetrability are the conditions applied at all solid boundaries. Fully developed flow is assumed at the outflow and plug flow is assumed at the inflow (neither are very realistic assumptions, but are adequate for the purpose at hand). At corners where a moving boundary intersects a stationary boundary, the non-physical singularity is removed by allowing slip in the neighborhood, in this case simply by taking the velocity to be zero at the corners, and equal to the lid speed at other nodes along the lid. The flow is characterized by Q, the flow rate, R, the ratio of speeds of the moving lids, and the aspect ratio (length divided by height) A.

Galerkin's method of weighted residuals is used with finite element basis functions to discretize Equation (1) and its boundary conditions [3,4]. Biquadratic basis functions are used

for the velocity, and linear discontinuous functions for the pressure. Bilinear basis functions are used to discretize the elliptic mesh generation equations described in the next two paragraphs.

The slot and dip coaters have free boundaries, the positions of which must be obtained as part of the solution. Elliptic mesh generation is employed in this case, in which a pair of elliptic partial differential equations in node-spacing potentials are solved to obtain the locations of the finite element nodes. The free surface is parameterized by the coupling of mesh generation to the physical problem through the free surface boundary conditions. The equations for mesh generation used here are those used by de Santos [5]: a pair of diffusion equations with variable coefficients,

$$\nabla \cdot D_{\xi}(\xi, \eta)\nabla\xi = 0, \qquad \nabla \cdot D_{\eta}(\xi, \eta)\nabla\eta = 0. \tag{2}$$

Together with boundary conditions, D_{ξ} and D_{η} control the steepness of gradients in the node-spacing potentials ξ and η, and thus the x- and y-spacing of nodes, which are equi-spaced in the potentials. Thus the diffusion coefficients were employed to concentrate nodes in regions of our choice.

A pair of boundary conditions on Equation (2) are required. One condition is obtained by applying boundary values of D_{ξ} and D_{η} that correspond to the desired node-spacing. Generally, hyperbolic functions were used to achieve a desired node-spacing potential along boundaries. The second condition is simply that the nodes stay on the boundary. For a fixed domain problem the boundary positions are parameterized by algebraic equations: lines, arcs of circles, etc. For free boundary problems, the kinematic boundary condition on the flow field ($\mathbf{n} \cdot \mathbf{u} = 0$) provides the appropriate parameterization of the boundary. It is through this boundary condition that the mesh equations become coupled to a viscous free surface flow [6].

The Galerkin–finite element method reduces the Navier–Stokes and elliptic mesh equations to the set of non-linear algebraic equations

$$\mathbf{R}(\mathbf{x}, \dot{\mathbf{x}}, \mathbf{p}) = 0, \tag{3}$$

where $\mathbf{x}$ is the solution vector, which consists of velocity and pressure unknowns, and in the case of the slot and dip coaters, the nodal locations. The time derivative of the solution vector is $\dot{\mathbf{x}}$, and $\mathbf{p}$ is a vector of the m parameters on which the problem depends.

Steady states of Equation (3), which are solutions with $\dot{\mathbf{x}} = 0$, are computed using Newton's method:

$$\mathbf{J}\delta\mathbf{x} = -\mathbf{R}, \qquad \mathbf{J} \equiv \frac{\partial \mathbf{R}}{\partial \mathbf{x}}, \tag{4}$$

$$\mathbf{x}^{i+1} = \mathbf{x}^{i} + \delta\mathbf{x}. \tag{5}$$

Iteration begins with an initial estimate $\mathbf{x}^0$ and is continued until Equation (3) is nearly satisfied: we required that both the L_2 norm of the residual vector $\mathbf{R}$ and the solution update $\delta\mathbf{x}$ be less than 10^{-4}. In the case of the slot coater, our initial estimate was a Stokes flow solution obtained with free surfaces replaced by fixed arcs of circles on which the gas exerts no shear stress. In the lid-driven cavity examples we began by neglecting inertia, in which case the problem is linear and no initial estimate is required.

2. TRACKING DESIRED FLOW STATES

Once a first solution to Equation (3) is obtained at any set of parameters, solutions at other parameter values are readily obtained by continuation. Continuation can be as simple as using the solution obtained at a nearby set of parameter values as the initial estimate for the new parameter values (called zeroth-order continuation). Generally it appears to be more efficient to use a first-order update, however (first-order continuation [7]):

$$\mathbf{J}(\mathbf{p})\mathbf{x}_\mathbf{p} = -\mathbf{R}_\mathbf{p}, \qquad \mathbf{R}_\mathbf{p} \equiv \frac{\partial \mathbf{R}}{\partial \mathbf{p}}, \tag{6}$$

$$\mathbf{x}^0(\mathbf{p} + \delta\mathbf{p}) = \mathbf{x}(\mathbf{p}) + \mathbf{x}_\mathbf{p}\,\delta\mathbf{p}, \qquad \mathbf{x}_\mathbf{p} \equiv \frac{\partial \mathbf{x}}{\partial \mathbf{p}}. \tag{7}$$

If Equation (4) is factorized with a direct solver, a set of m back-substitutions with $\mathbf{R}_\mathbf{p}$ can be used to update the initial estimate, which is a minor cost compared with the initial factorization. An advantage is gained here over iterative solvers, which require Equation (6) to be solved 'from scratch' m times.

$\mathbf{J}$ can be singular at isolated points along the solution branch. To handle these situations it is necessary to augment Equation (3) with additional constraints that regularize the system. In the case of a simple turning point, arc-length continuation can be used [7]. By adding constraints that characterize a turning point it is possible to track the location of the singular point in one parameter as a second parameter is varied [8]. Many additional references on the application of continuation methods to bifurcation analysis in fluid mechanics can be found in Reference [9].

In many cases the internal structure and external characteristics of a flow are of even greater interest than its singular states. To track such features, Equation (3) must be augmented with constraints that describe them. The procedure for doing so is described elsewhere [10]. One example in that paper shows how operating windows within which the upstream static contact line remains pinned to the corner of the slot coater die (a highly desirable flow state for processing) can be determined. Another example shows how the onset of separation at the upstream wall of a lid-driven cavity can be predicted. Here we show a parallel example, the calculation of conditions of flow separation within the feed channel of the slot coater.

The criterion of flow separation from a stationary wall is that the shear stress change sign smoothly with position along the wall. Thus a separation point must be a zero of the function $\tau_{\mathbf{tn}}(s) = \mathbf{tn}{:}\top$, where $\mathbf{t}$ and $\mathbf{n}$ are the unit vectors tangent and normal to the wall, and s is the co-ordinate along it. At the onset of separation $\tau_{\mathbf{tn}}$ must have a double root, so the pair of constraints that characterize the onset of separation at a boundary and augment Equation (3) is

$$\tau_{\mathbf{tn}}\big|_{s=s^*} = 0, \qquad \left.\frac{\mathrm{d}\tau_{\mathbf{tn}}}{\mathrm{d}s}\right|_{s=s^*} = 0. \tag{8}$$

Computing a zero of the second criterion of Equation (8) in a finite element discretization can be difficult. Derivatives of the velocity are discontinuous at element boundaries, which results in discontinuous terms in the Jacobian matrix. Such discontinuities cause serious problems for Newton's method. It is easier to track the circumstance where separation has just occurred, in which case two roots of $\tau_{\mathbf{tn}}$, a small distance δ apart, are sought:

$$\tau_{\mathbf{tn}}\big|_{s=s^*} = 0, \qquad \tau_{\mathbf{tn}}\big|_{s=s^*+\delta} = 0. \tag{9}$$

A value of 10^{-2} was used for δ. Were we to track the onset of separation at a free boundary at which the stress is zero everywhere, we would substitute the constraints that the velocity $\mathbf{u}$ and its derivative $d\mathbf{u}/ds$ are both zero; the idea, however, is the same.

In the general case, when n constraint equations $\mathbf{N}$ are needed to define the flow feature of interest, Equation (3) becomes

$$\mathbf{R}(\mathbf{x}, \mathbf{q}) = 0, \qquad \mathbf{N}(\mathbf{x}, \mathbf{q}) = 0, \tag{10}$$

where $\mathbf{q} \equiv (\mathbf{p}, \mathbf{s})$, and $\mathbf{s}$ is a vector of auxiliary parameters. If there are k auxiliary parameters, then $n-k$ parameters in $\mathbf{p}$ must be left unknown, or the system of Equation (10) is overspecified. In the current example there is one auxiliary parameter, which is the location of separation along the boundary.

The Newton step $(\delta\mathbf{x}, \delta\mathbf{q})$ is given by the solution of

$$\begin{bmatrix} \mathbf{J} & \mathbf{R}_\mathbf{q} \\ \mathbf{N}_\mathbf{x} & \mathbf{N}_\mathbf{q} \end{bmatrix} \begin{bmatrix} \delta\mathbf{x} \\ \delta\mathbf{q} \end{bmatrix} = - \begin{bmatrix} \mathbf{R} \\ \mathbf{N} \end{bmatrix}, \tag{11}$$

$$\mathbf{N}_{\mathbf{x}\equiv} \equiv \frac{\partial \mathbf{N}}{\partial \mathbf{x}}, \qquad \mathbf{N}_\mathbf{q} \equiv \frac{\partial \mathbf{N}}{\partial \mathbf{q}}, \qquad \mathbf{R}_\mathbf{q} \equiv \frac{\partial \mathbf{R}}{\partial \mathbf{q}}.$$

$\mathbf{J}$ is generally sparse and banded, but the augmented system is usually not, therefore, block elimination is required to exploit the sparsity of the original system:

$$\mathbf{J}\mathbf{w} = -\mathbf{R}, \qquad \mathbf{J}\mathbf{Y} = \mathbf{R}_\mathbf{q}, \qquad \mathbf{Y} \equiv (\mathbf{y}_1, \mathbf{y}_2, \ldots, \mathbf{y}_N), \tag{12}$$

$$\delta\mathbf{x} = \mathbf{w} - \mathbf{Y}\,\delta\mathbf{q}, \qquad \delta\mathbf{q} = -(\mathbf{N}_\mathbf{q} - \mathbf{N}_\mathbf{x}\mathbf{Y})^{-1}(\mathbf{N} + \mathbf{N}_\mathbf{x}\mathbf{w}). \tag{13}$$

After $\mathbf{J}\mathbf{z} = -\mathbf{R}$ is solved, the LU-decomposition of $\mathbf{J}$ can be back-substituted n times, once with each column vector of $\mathbf{R}_\mathbf{q}$, to get the column vectors of $\mathbf{Y}$. Though the inverse of a dense matrix appears in Equation (13), it is an $n \times n$ matrix that is generally much smaller than $\mathbf{J}$, and therefore is economical to compute. This is the procedure adopted here.

Figure 2 shows the dimensionless flow rate Q at the onset of separation in the feed channel of the slot coater. Conditions of the base flow are given in the figure caption. The ratio of Q to channel width is plotted versus channel width. Also shown is the location of separation, namely the distance upstream from the channel exit at which separation first occurs. All lengths in the figure are measured in units of the coating gap.

The ratio of Q to channel width is simply the dimensionless pressure gradient of fully developed flow in the channel. Figure 2 shows that the dimensionless pressure gradient at which separation occurs is nearly constant with respect to channel width, and that separation occurs near to the channel exit at all channel widths.

Use of continuation and solution tracking methods makes the accumulation of a large number of solutions convenient. Without further analysis, however, the mere accumulation of solutions is of little value. Some postprocessing tools that help to analyze these solutions systematically are presented in the next two sections.

3. PARAMETER SENSITIVITIES AND FREQUENCY RESPONSE

This section shows another use, apart from first-order continuation, of the linearized sensitivity of a solution to parameters $\mathbf{x}_\mathbf{p}$, gotten by solving Equation (6). When a direct solution method is used to obtain the factorization of $\mathbf{J}$ at the current parameter value, the cost to solve Equation (6) is much less than the cost of the factorization. The parameter sensitivities thereby obtained at little additional effort can provide considerable insight into the problem at hand.

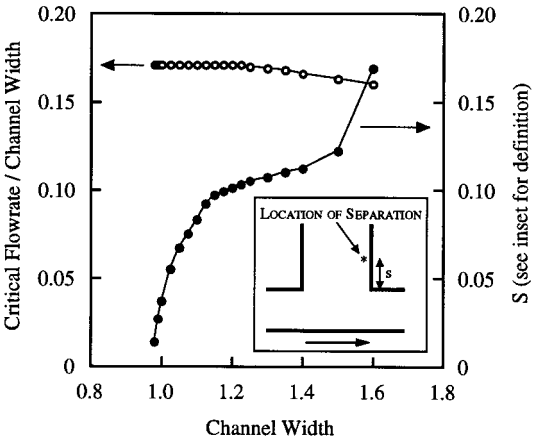

Figure 2. Tracking onset of separation in feed channel of a slot coater. Critical flow rate (○) and location of onset (●) versus channel width. $Re = 20$, $Ca = 0.125$, $St = 0.4$, $\theta_D = 120°$, $P_o = 36.36$, $\beta = 3 \times 10^{-2}$, $\lambda = 0.25$.

As an example, consider the progression from slot coating to dip coating, illustrated in Figure 3. Sartor and Scriven [1] showed that the slot-to-dip transition is characterized by the dependence of the coated layer thickness on the liquid pressure at the inlet. The slot coater is called a pre-metered flow, meaning that the final coated film thickness is controlled by the rate at which liquid is pumped through the inlet, which in turn is a function of the pressure at the inlet and the geometry of the coating die. The dip-coater is known as a self-metering flow: the final coated film thickness is controlled solely by the properties of the liquid and the rate at which the substrate, or web, is drawn from the bath. The only effect of a change in the inlet pressure is to affect the height to which the bath is filled with liquid. Sartor and Scriven charted the dependence of the final coated film thickness on the inlet pressure as a function of the coating gap. They found that this dependence correlates with the value of the Bond number: $Bo = \rho g L^2/\sigma$, which is the square of the ratio of the coating gap to the capillary length. At Bond numbers of order 10 and greater the flow is self-metering.

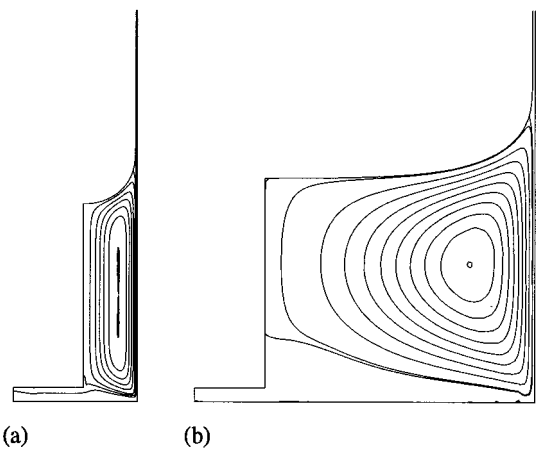

Figure 3. Streamlines in slot-to-dip transition: (a) narrow bath, $Bo = 1.33$, $Ca = 0.01$, $Re = 0.67$; (b) wide bath, $Bo = 32.7$, $Ca = 0.015$, $Re = 14.5$.

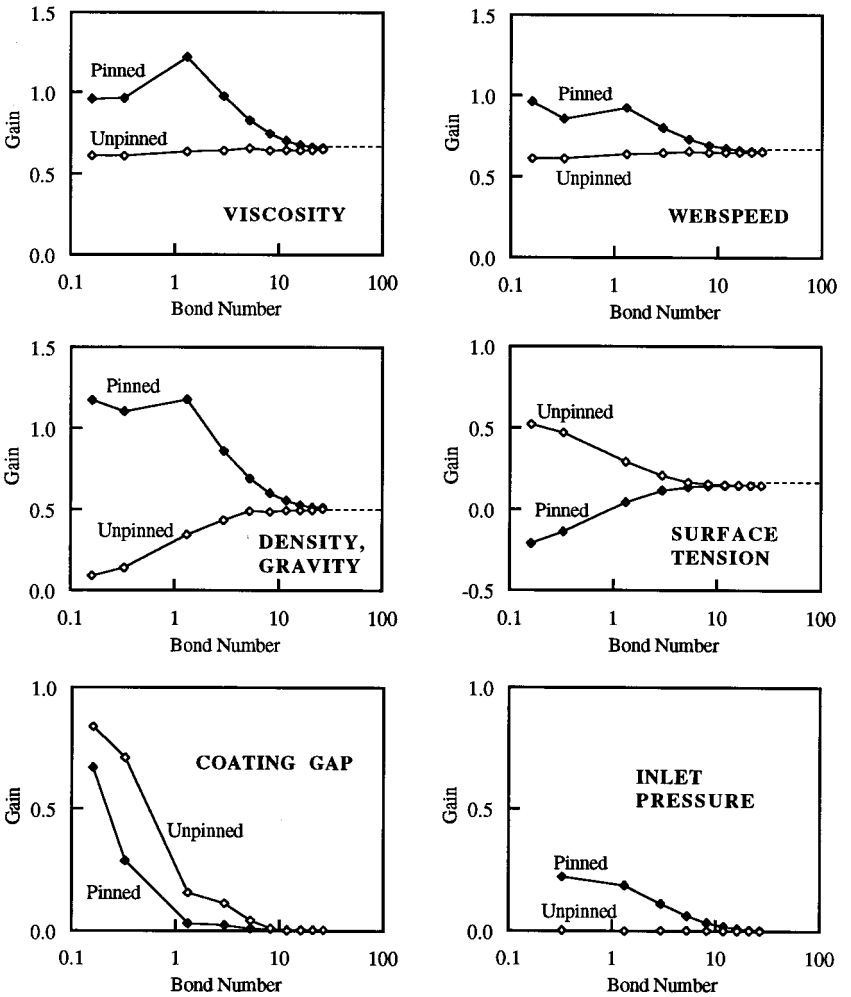

Figure 4. Gain, defined by Equation (14), versus Bond number for the slot-to-dip transition. $Ca = 0.01$, $Re = 0.0816$ at lowest Bond number, $Re = 16.65$ at highest Bond number (Re based on bath width L). Dashed lines show limiting values of the gain predicted using Equation (15).

To further understand the slot-to-dip transition, we studied the linearized sensitivity of the final film thickness to various parameters. Solutions were obtained over a range of coating gaps, characterized as a range of Bond numbers (no attempt was made to vary the capillary length, which is ≈ 0.2 cm in aqueous and organic coating liquids). Equation (6) was used to calculate the sensitivity of the final film thickness to perturbations of seven parameters: viscosity, density, gravity, surface tension, coating gap, web speed and inlet pressure. Two possibilities were considered: either the free surface is pinned at the corner of the coating die, or it is free to relocate elsewhere on the die surface but establishes a fixed contact angle whenever it does so. The latter case seems to be common in practical dip coating, whereas both cases seem common in slot coating (in slot coating, pinning is regarded as a desirable condition).

The calculated sensitivities are plotted in Figure 4 in the form of gain versus Bond number, where

$$\text{gain} \equiv \frac{p}{h}\frac{\partial h}{\partial p} = \frac{p}{(y_2 - y_1)}(y_{2,p} - y_{1,p}), \tag{14}$$

in which h is the final coated film thickness and p is the parameter. The y-locations of the web and free surface at the outflow are y_1 and y_2, and their parameter sensitivities are $y_{1,p}$ and $y_{2,p}$, which are obtained from the appropriate components of $\mathbf{x}$ and $\mathbf{x_p}$ respectively. This form of Equation (14) was chosen because if thickness varies with parameter to an exponent (power law dependence on p), the gain is equal to the exponent. Indeed, power law dependence on all parameters is predicted by Landau and Levich's [11] simple yet effective theory of dip coating at low capillary numbers and Reynolds numbers. That theory relates the final coated film thickness to the capillary number and capillary length:

$$h = aCa^{2/3}(\sigma/\rho g)^{1/2}, \tag{15}$$

in which a is a constant. Kheshgi *et al.* [12] have shown that Equation (15) is valid whenever $Ca \lesssim 0.01$, providing the coating gap is large enough (described as the case of an unconfined bath). Equation (15) is independent of the coating gap, the inlet pressure, and the Reynolds number.

Figure 4 shows the gains predicted by Landau and Levich's approximation as dashed lines. The gains computed from solutions to the Navier–Stokes equations are shown by symbols, in both pinned and unpinned cases. A contact angle of 90° was used in the unpinned case. The results indicate that the Landau and Levich approximation applies, providing the Bond number is greater than about 10, in this case in which $Ca = 0.01$. The transition to this open-bath dip coating limit is quite different in the pinned and unpinned cases, however. In particular, the thickness of the coating in the unpinned case is not a function of the inlet pressure at any Bond number; hence, the flow is self-metering at all Bond numbers. In the pinned case, the influence of inlet pressure is significant at Bond numbers < 10, under which condition it is possible to pre-meter the flow to a desired rate.

When the coating gap is of the order of the capillary length or less, the coating gap exerts a strong influence on the final coated film thickness, which is the effect of bath confinement noted by Deryagin and Levi [13]. In the unpinned case, however, the effect is stronger and occurs up to somewhat larger Bond numbers than in the pinned case. In the pinned case there is almost no effect at all unless the coating gap is less than the capillary length, whereas in the unpinned case, there is a modest effect at a coating gap that is two or three times the capillary length.

It should be noted that the effects of coating gap and inlet pressure depend strongly on the shape of the coating die. In the unpinned case, for instance, if the downstream die lip is inclined with respect to the web rather than parallel to it, the bath width is no longer constant. A change in the inlet pressure will cause the meniscus to relocate to a point at which the bath width is changed. The change in bath width corresponds to a change in the shape of the meniscus, the effect of which is to change the final coated film thickness when the Bond number is less than about ten. In such a case it is possible to pre-meter the flow, unlike the case shown in Figure 4. A thorough discussion of these effects is beyond the scope of this paper, however. The interested reader is referred to Reference [14] for more information on the effects of die geometry in slot coating.

To gain further insight into the slot-to-dip transition, we studied the dynamic responses of the solution to the time-periodic sinusoidal variation of parameters:

$$\delta p(t) = \epsilon \exp(i\omega t), \tag{16}$$

where ω is the frequency and ϵ is the amplitude of the disturbance to the chosen parameter p (only the real part of Equation (16) is of interest). To first order in $\delta\mathbf{x}$, the response to a small disturbance around a steady state $\mathbf{x}_o$ is governed by the linearization of Equation (3):

$$\mathbf{J}(\mathbf{x}_o, 0, \mathbf{p_o})\,\delta\mathbf{x} + \mathbf{M}(\mathbf{x}_o, 0, \mathbf{p_o})\,\delta\dot{\mathbf{x}} + \mathbf{R_p}(\mathbf{x}_o, 0, \mathbf{p_o})\,\delta p = 0, \qquad \mathbf{M} = \frac{\partial \mathbf{R}}{\partial \dot{\mathbf{x}}}. \tag{17}$$

$\mathbf{M}$ is the so-called mass matrix, the matrix of basis function overlaps in the sense of inner products of the finite element basis functions (the equivalent matrix when the equations are approximated by finite differences is the identity matrix).

Assuming that the base flow $\mathbf{x}_o$ is stable (and thus the complementary part of the solution to Equation (17) decays with time), the response to the disturbance asymptotically approaches a particular solution of the form

$$\delta\mathbf{x} = \epsilon\mathbf{z} \exp(i\omega t), \tag{18}$$

where $\mathbf{z}$ is the complex amplitude of the response. Substituting the assumed forms of δp and $\delta\mathbf{x}$ into Equation (17) gives

$$(\mathbf{J} + i\omega\mathbf{M})\mathbf{z} = -\mathbf{R}_p. \tag{19}$$

Equation (19) is solved to obtain $\mathbf{z}$, which is used to compute the time periodic response according to

$$\mathbf{x}(t) = \mathbf{x}_o(p_o) + \Re(\epsilon\mathbf{z} \exp[\omega t]). \tag{20}$$

The response of component j of the solution $\mathbf{x}(t)$ can be characterized by an amplitude $|z_j|$ and phase shift θ:

$$x_j(t) = x_{j,o} + \epsilon|z_j| \cos[(\omega + \theta)t], \tag{21}$$

where $|z_j| = \sqrt{z_{j,\Re^2} + z_{j,\Im^2}}$ and $\theta = \arctan(z_{j,\Im}/z_{j,\Re})$. Usually the quantity of interest is the amplitude. Further details are provided by Christodoulou [9], who studied the response of single and two-phase slide coating flows to several parameters.

Figure 5 shows the frequency response of a dip coater to forced variations in the inlet pressure and web position normal to the web, in the form of gain versus frequency. The gain is computed from

$$\text{gain} \equiv \frac{p_o}{h_o}\left|\frac{\delta h}{\delta p}\right| = \frac{p_o}{(y_{2,o} - y_{1,o})}\,|y_{2,p} - y_{1,p}|. \tag{22}$$

The meanings of the symbols in Equation (22) are the same as in Equation (14), except that here $y_{j,o}$ refers to components of the steady state solution $\mathbf{x}_o$, and $y_{j,p}$ refers to components of the complex response $\mathbf{z}$. Notice that at $\omega = 0$, Equation (6) is recovered from Equation (19), $\mathbf{z}$ is equivalent to $\mathbf{x_p}$, and Equation (14) is recovered from Equation (22). Hence the gains plotted in Figure 4 can be called zero-frequency gains.

The free surface is unpinned in both cases shown in Figure 5. Two gap widths are considered: a narrow bath in which $Bo = 1.33$, i.e. gap width approximately equal to the capillary length, and a wide bath in which $Bo = 32.7$, i.e. gap width much larger than capillary length. In both cases the most dangerous frequencies occur in the range of 1–10 Hz. At the most dangerous frequencies, the influence of web vibration is quite large. In the narrow bath the amplitude of variation in the coated film thickness is four times the amplitude of the

variation in web position. It is no surprise that the gain is large in the narrow bath, given that bath confinement has a significant effect at zero frequency. It is somewhat surprising, however, that a gain of nearly two is observed at the most dangerous frequency in the wide bath, in which there is essentially no effect of bath confinement at zero frequency. On this basis we surmise that the primary cause of coated film thickness variation is not due to the bath confinement effect on the shape of the free surface, but due rather to the pumping of fluid from the bath into the film region downstream of the web.

Pressure fluctuations cause a gain of ≈ 0.3 at the most dangerous frequency in the narrow bath, and virtually no gain at all at the most dangerous frequency in the wide bath. We suspect that perturbations in the inlet pressure are damped before reaching the free surface, whereas perturbations of the coating gap act directly on the bath as a whole and thus are relatively undamped at the free surface.

Figure 5 also shows the leading eigenvalues, plotted in the form of frequencies, obtained by solving the generalized eigenproblem associated with sudden small disturbances of the flow (linearized stability theory), as described by Christodoulou and Scriven [15]. According to the theory, the response of a steady state solution $\mathbf{x}_o$ to a small disturbance $\delta\mathbf{x}(0)$ is given by

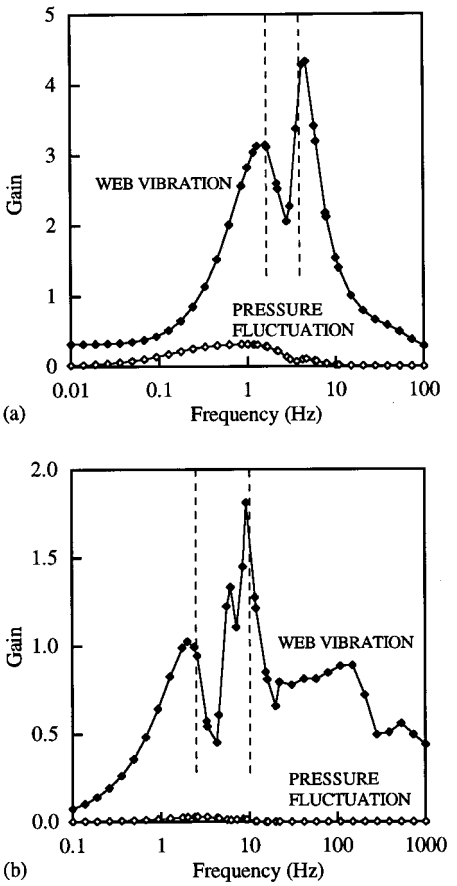

Figure 5. Frequency response of dip coater to forced variations in web vibration and inlet pressure: (a) narrow bath, $Bo = 1.33$, $Ca = 0.01$, $Re = 0.67$; (b) wide bath, $Bo = 32.7$, $Ca = 0.015$, $Re = 14.5$. Vertical lines indicate frequencies of leading eigenmodes.

$$\delta \mathbf{x}(t) = \sum_{j=1}^{N} \epsilon_j \mathbf{z}_j \exp(\omega_j t), \tag{23}$$

where N is the number of unknowns (and therefore the number of normal modes $\mathbf{z}_j$) of the discretized problem. The normal modes and associated eigenvalues ω_j are obtained by solving

$$\mathbf{J}(\mathbf{x}_o, 0, \mathbf{p}_o) = -\omega_j \mathbf{M}(\mathbf{x}_o, 0, \mathbf{p}_o)\mathbf{z}_j, \tag{24}$$

which is simply Equation (17) with Equation (23) substituted for $\delta \mathbf{x}$, and δp set to zero. Arnoldi's method is used to obtain a few eigenvalues of the largest real part, using the techniques described in Reference [15]. As expected, these frequencies closely match the most dangerous frequencies predicted by the frequency response analysis.

4. PROBING THE STRUCTURE OF FLOWS

Often it is the qualitative features of a flow that are of the greatest interest. In many cases, for example, it is particularly important to know whether flow separation occurs. There are a great many flows in which separation occurs at a boundary. Separation also occurs within the domain in many situations, however, as demonstrated by Jeffrey and Sherwood [16]. Other fascinating examples that exhibit internal separation are shown by Coyle and Scriven [2], in a simulation of a roll-coater, and by Goodwin and Schowalter [17], in a simulation of a pair of submerged, confined jets (the latter used the algorithm developed here to produce the figures). These examples, along with the results shown below, demonstrate the importance of locating all separation points in a flow, both internal and at the boundaries. Merely selecting a number of equally spaced contour values, which is the customary way to plot streamlines, often fails to reveal internal separation points, however. What is needed is a systematic way to locate all separation points in a flow. Such a method is described here.

In steady incompressible flows in two dimensions, there are two types of stagnation points: separation points, and vortex centers. Both can be characterized as critical points of the streamfunction ψ, defined by the condition that $\nabla\psi = \mathbf{0}$ (which implies $\mathbf{u} = \psi_y \mathbf{i} - \psi_x \mathbf{j} = \mathbf{0}$). The Hessian $H(\psi) = \psi_{xx}\psi_{yy} - \psi_{xy}^2$ discriminates the type of critical point: $H(\psi) > 0$ at an extremum, which is a vortex center, and $H(\psi) < 0$ at a saddle, which is a separation point. Jeffrey and Sherwood used these criteria to locate all stagnation points, from which they constructed figures that show vortex centers and separation streamlines in various flows. Such figures, which we call critical point plots, reveal whether separation occurs, and whether trapped regions of fluid with infinite residence time are present in throughflows.

To understand the connection between the critical points of a flow and its topology, we consider particle paths, which are described by a conservative autonomous planar dynamical system [18]: $\mathrm{d}\mathbf{y}(\mathbf{y}_o)/\mathrm{d}t = \mathbf{u}$, where $\mathbf{y}(\mathbf{y}_o)$ is the locus of points along the particle path through the point $\mathbf{y}_o$. The quantity that is conserved along the particle paths is the streamfunction, because the particle paths coincide with the streamlines in a steady incompressible flow in two dimensions. Also, critical points of the streamfunction are equilibrium points of the particle paths. Stagnation points are either stable (vortex centers) or unstable (separation points) equilibria. Separation streamlines are unstable manifolds that divide the flow into stable and unstable regions of particle location. Within stable regions the fluid residence time is infinite. According to the theory of dynamical systems, the topology of a solenoidal velocity field is completely determined by the locations and types of its equilibria, and its unstable manifolds. Thus, by locating all stagnation points and separation streamlines, the topology of the flow is known.

A change in flow topology occurs at a critical point if $H(\psi)$ changes sign when some parameter upon which the flow depends is varied. It is possible for $H(\psi)$ to go through zero without changing sign, which also marks a change in flow topology. Hence parameter values at which $H(\psi) = 0$, sometimes referred to as bifurcation points, are of special interest (here the term bifurcation refers to a change of stability of the equations that describe the particle paths, rather than a change in stability of the Navier–Stokes equations). Such bifurcations often result in a change of the number and type of critical points, but bifurcations are also possible in which only the unstable manifolds change [18].

Critical point concepts in fluid dynamics are reviewed by Perry and Chong [19]. They discuss the classification of critical points in three-dimensional flows (where many more types occur than in the two-dimensional case), and review previous attempts to analyze fluid flows using these concepts. Most attempts have relied on Taylor expansions about the critical point. However, these local analyses have been of limited use in determining the topology of flows.

Systematic attempts to analyze the topology of numerically generated flow solutions first appeared in the late 1980's and are briefly reviewed by Globus *et al.* [20]. They describe a software tool (TOPO) developed for visualizing the topology of three-dimensional vector fields based on critical-point analysis. They demonstrate the use of TOPO in the analysis of data sets from fluid dynamics simulations of some three-dimensional flows. TOPO makes a significant step towards the systematic computation of the complete topology of three-dimensional flows, a very difficult problem, but still retains considerable limitations. Here we restrict ourselves to the easier task of analyzing two-dimensional incompressible flows.

The first step to locating critical points is to find all stagnation points. The point at which the velocity goes to zero at a boundary is easily found, since its value can be always be parameterized by one co-ordinate (the arc-length along the boundary), which reduces the problem to finding the root of a one-dimensional equation. In the Galerkin–finite element method employed here, all that is required is to test for roots element-by-element by solving an appropriate quadratic equation. This method fails at no-slip boundaries, however, since all points at the boundary have zero velocity, but not all are critical points. In this case the appropriate criterion is that the shear stress changes sign smoothly with position along the wall. Thus, a critical point must be a zero of the function $\tau_{\mathbf{tn}}(s) = \mathbf{tn}{:}\top$, where $\mathbf{t}$ and $\mathbf{n}$ are the unit vectors tangent and normal to the wall, and s is the co-ordinate along it. The task reduces to finding the roots of a one-dimensional function.

The velocity within the domain is a function of two space co-ordinates; therefore, in order to find the points of zero velocity, the roots of a two-dimensional system of equations are required, a task for which no method guarantees success. Consequently, locating stagnation points within the domain is considerably more difficult than on the boundaries. A robust alternative to finding zeroes of the velocity components is to find points at which the speed is a minimum. Minima at which the speed is less than a small tolerance are identified as stagnation points. In practice we find that this tolerance can be made quite small. We find that a tolerance 10^{-10} is feasible for problems in which the average velocity is $\mathcal{O}(1)$.

The method used here locates minima of a multidimensional system via the downhill simplex method [21]. This method was chosen because it requires no derivative information and thus is simpler to implement than other methods. The method is slow, however, typically requiring as long to generate a critical point plot as it took to obtain the solution in the first place. The cause, of course, is a linear rate of convergence. Methods that utilize derivative information can give a higher order rate of convergence, and should be much faster, but none were tested.

Generally, methods used to locate minima of multivariable functions are iterative, and usually are only guaranteed to find a local minimum. The method is likely to find a local

minimum near the initial estimate of its location. To ensure that all minima are found, the minimization is repeated with its initial guess taken as the center of each of the elements. Since the low-order basis functions used here can resolve no more than one stagnation point in a single element, this procedure generally is sufficient to find all critical points (except, on occasion, corner vortices that are contained within a single element).

When all the stagnation points are found, they must be identified as vortex centers or separation points. The Hessian of the streamfunction could be tested, but estimating second derivatives of the streamfunction (itself a derived quantity) is not sufficiently accurate when applied to a low-order polynomial approximation with limited differentiability (in our case, biquadratic basis functions). In many of the cases tested, the computed Hessian misidentified the type of critical point. An alternate, robust method to identify critical points in finite element calculations is as follows: (i) identify which stagnation points are vortex centers by using a minimization algorithm to locate all extremes of the streamfunction (to find maxima we first change the sign of the streamfunction, then locate the minima); (ii) infer that the critical points that are not extremes of the streamfunction must be separation points.

Recent papers by Shankar [22] and Hellou and Coutanceau [23] present computational methods without which they claim it would be impossible to reliably and easily discern critical points. Both methods are based on global basis functions that are tailored in some sense to a particular type of flow. Thus neither method is particularly general. Our method for locating critical points does not rely on use of global basis functions, however, and thus is applicable regardless of the basis function choice.

The lid-driven cavity with throughflow (Figure 1c) illustrates how critical point plots can reveal flow structure that otherwise would pass unnoticed. The lower 10% of the left boundary is open to inflow, and the upper 10% of the right boundary is open to outflow. Figure 6 shows streamline plots at three flow rates, with and without the critical points displayed, at a speed ratio of one. Thirty streamlines are plotted in the conventional manner, at equal intervals between the maximum and minimum values. Without showing critical points, virtually no differences can be detected among the three cases. With critical points, it is clear that significant regions of trapped fluid are present at the lowest flow rate shown, $Q = 0.3258$. At a slightly higher flow rate, $Q = 0.3335$, regions of trapped fluid are present, but are so small that the symbols marking the vortex centers and separation points (which lie almost on top of each other) obscure them in the figure. At a slightly higher flow rate the regions of trapped fluid disappear. Over 400 streamlines would be required (plotted at equal intervals) to reveal the recirculations shown in the $Q = 0.3258$ case. In the $Q = 0.3335$ case, over 50 000 would be required.

Presumably, the flow in the limit as the cavity grows infinitely long is strictly parallel rectilinear flow, the superposition of plane Couette and plane Poiseuille flow that satisfies the boundary conditions at the top and bottom walls and passes the flow rate Q. We refer to this as the Couette–Poiseuille limit. In this type of flow, when the speed ratio equals one, flow rates less than one-third are accompanied by backflow. The flow far from the ends of a finite length cavity should closely resemble the Couette–Poiseuille limit. In a long cavity, therefore, the onset of backflow at the center of the cavity should occur at a flow rate near to one-third, which indeed is the case, as shown by Figure 6.

In the Couette–Poiseuille limit, regions of backflow are separated from forward flow by stagnation streamlines (along which the velocity is zero). Figure 6 shows that when there is backflow in a finite length cavity, the incoming fluid divides into three streams that take separate paths through the cavity. There are no stagnation streamlines, but there are stagnation points that lie very close to the locations of the stagnation streamlines predicted in

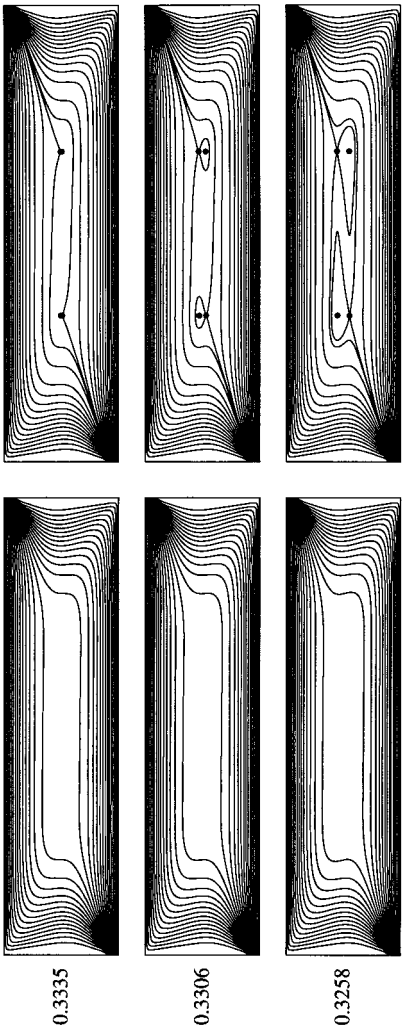

Figure 6. Streamlines versus flow rate in lid-driven cavity with throughflow. Top and bottom walls move from left to right. Results at each flow rate are shown both with and without critical points. Speed ratio $R = 1$, aspect ratio $A = 4$, $Re = 0$.

the Couette–Poiseuille limit. Two of these streams flow forward along the walls. The third stream travels an S-shaped path through the cavity. It is along this path that backflow occurs.

The flow rate at which the onset of backflow occurs is a function of the speed ratio. In the Couette–Poiseuille limit it can be shown that the critical flow rate is related to the speed ratio by

$$\frac{Q}{(1+R)/2} = \frac{2}{3}\left[1 - \frac{\sqrt{R}}{1+R}\right]. \tag{25}$$

The uppermost curve in Figure 7 corresponds to Equation (25). Galerkin–finite element solutions of Equation (1) for a cavity with an aspect ratio equal to four show that the onset of backflow—and therefore the transition from a one-path state to a three-path state—matches the Couette–Poiseuille prediction of the critical flow rate to within 1%.

At a speed ratio equal to one and flow rate equal to one-ninth, another transition occurs, to a state in which the incoming fluid passes through the cavity in a single stream and large recirculations appear. This is the lower one-path state shown in Figure 7. All incoming fluid travels through the cavity along the S-shaped path. The flow rate at which this transition occurs is equal to the flow rate that circulates around each of two symmetric vortices that fill the cavity when there is no throughflow. At a speed ratio not equal to one, the two vortices that fill the cavity in the no-throughflow case no longer are symmetric; therefore each vortex circulates a different flow rate. One of these critical flow rates is given by

$$\frac{Q}{(1+R)/2} = \frac{4+6R-4\sqrt{1+3R}}{9(1+R)}. \tag{26}$$

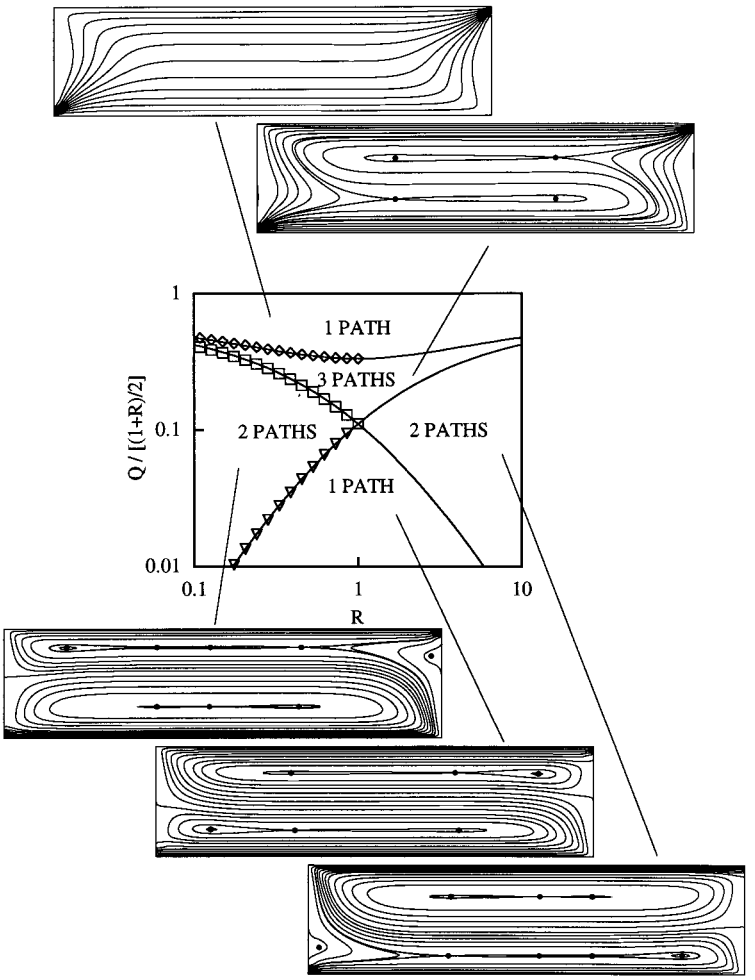

Figure 7. Phase diagram of flow topology of lid-driven cavity with throughflow. The upper curve is Equation (25), and the lower curves are Equation (26) (the lower curve with negative slope is gotten from Equation (26) with $1/R$ substituted for R). Symbols show transitions found from solutions of the Navier–Stokes equations. $Re = 0$, aspect ratio $A = 4$.

The other critical flow rate is given by the same expression with $1/R$ substituted for R. These two expressions give the lower curves in Figure 7, which cross at $R = 1$. Again, Galerkin–finite element solutions of Equation (1) for a cavity with an aspect ratio equal to four match the Couette–Poiseuille prediction of the critical flow rate to within 1%. Transitions from a three- to a two-path state, and from a two- to a one-path state, occur at these critical flow rates, as illustrated in Figure 7. What is remarkable about these results is that the limiting behavior, specifically of an infinitely long cavity, accurately matches the Navier–Stokes solutions for the two-dimensional flow in a rather short cavity.

5. CONCLUDING REMARKS

It is common to think of computational fluid dynamics as being divided into three major tasks: constructing a discretization (e.g. generating a mesh), solving the discretized Navier–Stokes equations, and postprocessing the solution to obtain graphical representations of the flow, such as streamline and velocity vector plots. It is generally recognized that there is a strong coupling between mesh generation and solving the discretized equations when the mesh is unknown *a priori* (as is the case in the dip and slot coating examples). Postprocessing is usually treated as being independent of the other tasks, however. Indeed, this is the case when line, contour, or vector plots of pointwise measures of the flow (which can be computed explicitly from the solution vector) are all that is needed. Such graphical representations only require information that can be directly derived from the solution.

In contrast, the only method presented here that can be applied given only the solution vector is computation of critical point plots. Evaluation of parameter sensitivities and frequency response to parameter perturbations requires computation of the Jacobian matrix (as does linearized stability analysis). Thus these methods are coupled in some sense to the solution of the discretized equations. An even more intimate coupling is required to track desired flow states, in that a postprocessing result is obtained as part of the solution. It has been shown here that by expanding the notion of postprocessing, fruitful insight can be gained that would otherwise be difficult to glean using conventional postprocessing tools.

ACKNOWLEDGMENTS

The author gratefully acknowledges the assistance of Ralph T. Goodwin III in implementing the algorithm presented in Section 4 of the paper.

REFERENCES

1. L. Sartor and L.E. Scriven, 'The progression from dip coating to slot coating: what controls film thickness', *AIChE Annual Meeting*, Chicago, November 11–16, Paper 163d, 1990.
2. D.J. Coyle, C.W. Macosko and L.E. Scriven, 'Film-splitting flows in forward roll coating', *J. Fluid Mech.*, **171**, 183 (1986).
3. T.J.R. Hughes, *The Finite Element Method*, Prentice Hall, Englewood Cliffs, NJ, 1987.
4. G. Dhatt and G. Touzot, *The Finite Element Method Displayed*, Wiley, New York, 1984.
5. J.M. de Santos, 'Two-phase cocurrent downflow through constricted passages', *Ph.D. Thesis*, University of Minnesota, 1991. Available from University Microfilms International, Ann Arbor, MI 48106.
6. K.N. Christodoulou and L.E. Scriven, 'Discretization of free surface flows and other moving boundary problems', *J. Comput. Phys.*, **99**, 39 (1992).
7. J.H. Bolstad and H.B. Keller, 'A multigrid continuation method for elliptic problems with folds', *SIAM J. Sci. Stat. Comput.*, **7**, 1081 (1986).

8. G. Ponisch and H. Schwetlick, 'Computing turning points of curves implicitly defined by nonlinear equations depending on a parameter', *Computing*, **26**, 107 (1981).
9. K.N. Christodoulou, 'Computational physics of slide coating flow', *Ph.D. Thesis*, University of Minnesota, 1990. Available from University Microfilms International, Ann Arbor, MI 48106.
10. A. Yeckel and L.E. Scriven, 'Multiparameter continuation methods for tracking desired flow states', *Supercomputing '92 Conference of the IEEE/ACM Proceedings*, Minneapolis, November 16–20, 1992, pp. 142–151.
11. L. Landau and B. Levich, 'Dragging of a liquid by a moving plate', *Acta Phys-chim. URSS*, **17**, 42 (1942).
12. H.S. Khesghi, S.F. Kistler and L.E. Scriven, 'Rising and falling film flows: viewed from a first-order approximation', *Chem. Eng. Sci.*, **47**, 683 (1991).
13. B.M. Deryagin and S.M. Levi, *Film Coating Theory*, The Focal Press, New York, 1959. (English translation published 1964).
14. B.G. Higgins, 'Capillary hydrodynamics and coating beads', *Ph.D. Thesis*, University of Minnesota, 1980. Available from University Microfilms International, Ann Arbor, MI 48106.
15. K.N. Christodoulou and L.E. Scriven, 'Finding leading modes of a viscous free surface flow: An asymmetric generalized eigenproblem', *J. Sci. Comput.*, **3**, 355 (1988).
16. D.J. Jeffrey and J.D. Sherwood, 'Streamline patterns and eddies in low-Reynolds-number flow', *J. Fluid Mech.*, **96**, 315 (1980).
17. R.T. Goodwin III and W.R. Schowalter, 'Interactions of a pair of submerged jets in a channel: Solution multiplicity and linear stability', *J. Fluid Mech.*, **313**, 55 (1996).
18. J. Hale and H. Koçak, *Dynamics and Bifurcations*, Springer, New York, 1991.
19. A.E. Perry and M.S. Chong, 'A description of eddying motions and flow patterns using critical point concepts', *Annu. Rev. Fluid Mech.*, **19**, 125 (1987).
20. A. Globus, C. Levit and T. Lasinski, 'A tool for visualizing the topology of three-dimensional vector fields', *NASA Report RNR-91-017*, 1991.
21. J.A. Nelder and R. Mead, 'A simplex method for function minimization', *Comput. J.*, **7**, 308 (1965).
22. P.N. Shankar, 'The eddy structure in Stokes flow in a cavity', *J. Fluid Mech.*, **250**, 371 (1993).
23. M. Hellou and M. Coutanceau, 'Cellular Stokes flow induced by rotation of a cylinder in a closed channel', *J. Fluid Mech.*, **236**, 557 (1992).

